

Effects of mass loss for highly-irradiated giant planets

W. B. Hubbard*, M. F. Hattori*, A. Burrows†, I. Hubeny†, and D. Sudarsky†

*Lunar and Planetary Laboratory, University of Arizona, Tucson AZ 85721, USA

†Department of Astronomy, University of Arizona, Tucson AZ 85721, USA

Abstract

We present calculations for the evolution and surviving mass of highly-irradiated extrasolar giant planets (EGPs) at orbital semimajor axes ranging from 0.023 to 0.057 AU using a generalized scaled theory for mass loss, together with new surface-condition grids for hot EGPs and a consistent treatment of tidal truncation. Available theoretical estimates for the rate of energy-limited hydrogen escape from giant-planet atmospheres range over four orders of magnitude, when one holds planetary mass, composition, and irradiation constant. Yelle (2004, *Icarus* 170, 167-179) predicts the lowest escape rate. Baraffe *et al.* (2004, *A&A* 419, L13-L16) predict the highest rate, based on the theory of Lammer *et al.* (2003, *Astrophys. J.* 598, L121-L124). Scaling the theory of Watson *et al.* (1981, *Icarus* 48, 150-166) to parameters for a highly-irradiated exoplanet, we find an intermediate escape rate, $\sim 10^2$ higher than Yelle's but $\sim 10^2$ lower than Baraffe's. With the scaled Watson theory and the scaled Yelle theory we find modest mass loss, occurring early in the history of a hot EGP. Particularly for the Yelle theory, the effect of tidal truncation sets the minimum mass limit, well below a Saturn mass for semimajor axes ≥ 0.023 AU. This contrasts with the Baraffe model, where hot EGPs are claimed to be remnants of much more massive bodies, originally several times Jupiter and still losing substantial mass fractions at present.

Key words: extrasolar planets, jovian planets, thermal histories

1. Introduction

At present considerable uncertainty exists as to whether extrasolar giant planets (EGPs) are likely to suffer appreciable mass loss over their lifetime when subjected to high levels of XUV irradiation from their host star. A major question concerning the origin of short-period (period $P \sim$ days, semimajor axis $a \sim$ few $\times 10^{-2}$ AU) EGPs concerns this point: do short-period (hot) EGPs originate with their presently-observed masses at $a \sim 10$ AU and migrate rapidly to $a \sim$ few $\times 10^{-2}$ AU without appreciable mass loss, or were the original bodies several times more massive, suffering continual rapid mass loss throughout their evolution? The latter scenario, advocated by Baraffe *et al.* (2004), implies that the observed hot EGPs are remnants of much more massive objects and are continuing to lose mass at a significant rate at present. However, Yelle's (2004) theory gives a very different history for hot EGPs: As we show in this paper, his theory implies that only hydrogen-rich EGPs with mass $M < 0.1 M_J$ (where M_J = Jupiter's mass) will be affected by mass loss.

We do not present here any independent calculations of the escape rate Φ (molecules $\text{cm}^{-2} \text{s}^{-1}$) as a function of Q_0 (erg $\text{cm}^{-3} \text{s}^{-1}$), the volume-heating rate of the

planetary atmosphere due to absorption of stellar XUV radiation. For energy-limited escape, the two quantities are proportional. As we discuss below, for fixed XUV irradiation from a solar-type star, the Yelle theory gives a proportionality constant, and therefore an atmospheric escape rate, that is 10^{-4} of the escape rate predicted by Baraffe *et al.* Tidal effects have been extended to the Lammer formulation (Jaritz *et al.* 2005), but not explicitly in the Yelle theory. The purpose of the present paper is to present, side by side, the implications of the Baraffe and Yelle theories by consistently including tidal effects in energy-limited escape for both theories. An older theory of energy-limited hydrogen escape from the Earth has been presented by Watson *et al.* (1981). For further comparison, we scale the Watson theory to hot EGPs, including tidal effects, and compare it with the Baraffe and Yelle theories.

2. Scaling Relations

2.1. Effect of tides on atmospheric binding

The critical parameter for the binding of the EGP atmosphere is usually written as (Yelle 2004)

$$\lambda = \frac{GMm}{kTr}, \quad (1)$$

where G is the gravitational constant, m is the molecular mass (2 amu for H_2), k is Boltzmann's constant, T is the atmospheric temperature, and r is the atmospheric radius. For a planet at great distance from its primary, one may write

$$\lambda = \frac{mV_0}{kT}, \quad (2)$$

where V_0 is the gravitational potential of the atmospheric layer and $E_B = mV_0$ is the gravitational binding energy of a molecule. In energy-limited escape, a certain fraction of the energy from the star impinging on the EGP atmosphere, averaged over the stellar spectrum, removes a hydrogen molecule from the atmosphere by supplying it with kinetic energy $> mV$. The efficiency of this process is much less than unity because only XUV photons are effective in heating the upper atmosphere. The efficiency is reduced further because part of the XUV photon energy drives dissociation, ionization, and other reactions without removing the reaction products from the atmosphere. Let the efficiency of this process be

$$\varepsilon = \frac{\Phi E_B}{S_*}, \quad (3)$$

where S_* is the “solar” (or stellar) constant, the photon power normally incident on the EGP atmosphere at the planet's orbital radius a . The predicted efficiency factor ε ranges from $\sim 10^{-4}$ for the Baraffe model (meaning that for every 10^4 ergs of stellar photon energy averaged over wavelength that impinge on the EGP atmosphere, ~ 1 erg is available to remove a hydrogen molecule) to $\sim 10^{-8}$ for the Yelle model.

The above arguments require modification when a significant tidal potential is present, i.e., when r is only a factor ~ 2 to 3 smaller than r_H , where r_H is the radius of the planet's Hill sphere. For example, this will be the case for an EGP orbit about a $1 M_\odot$ (solar mass) star with a semimajor axis $a \sim 0.023$ AU. When this is the case, we

recognize that the gravitational binding energy of a molecule is no longer $E_B = mV(r)$, but rather

$$E_{B,\text{mod}} = mV_{\text{mod}}(r) - mV_{\text{mod}}(L1) = m\Delta V_{\text{mod}}, \quad (4)$$

where V_{mod} is the usual modified gravitational potential in the planet's frame, including the stellar and planetary gravitational potentials and the effective rotational potential. At the L1 point between the planet and star (as well as at the nearly-symmetric L2 on the other side of the planet), molecules are not gravitationally bound to the planet and can go into independent orbit about the star. Strictly speaking, when r is very close to r_H , effectively close to L1 or L2, the planet is strongly distorted from a spherical shape and the modified potential should include this distortion. However, as this limit is approached, mass loss occurs very quickly, by virtue of a modified binding parameter,

$$\lambda_{\text{mod}} = \frac{E_{B,\text{mod}}}{kT} \rightarrow 0, \quad (5)$$

and imprecision in the evaluation of $E_{B,\text{mod}}$ will affect the mass limit only slightly.

In summary, the effect of tides is represented in the scaled theory by multiplying the escape rate $\Phi(Q_0)$ by the tidal enhancement factor $\tau = V_0/\Delta V_{\text{mod}} > 1$. Figure 1 gives an example of the calculation of the tidal enhancement factor for EGPs at an orbital radius $a = 0.023$ AU, equal to that of OGLE-TR-56b (whose mass $M = 1.45 \pm 0.23$ M_J; Bouchy *et al.* 2005), for a 1-M_⊕ primary star. Note that the actual mass of OGLE-TR-56 is 1.04 ± 0.05 M_⊕.

Figure 1 illustrates the point that the tidal limit is of course a function of the planetary radius r , which in turn is a function of the internal entropy of the EGP. The solid curve represents the relative reduction in the binding energy for an internal entropy corresponding to an isolated cooling age of 1 Ma, and the dotted curve corresponds to an age of 5 Ma. The curves osculate the abscissa at $M \sim 0.15$ M_J, which corresponds roughly to the point at which the planet would fill its Roche lobe; the atmosphere is completely unbound at this point. The curves turn back up for smaller masses, but there is no physical significance to this branch. Further discussion of the tidal limit is presented in Section 3.

2.2. Description of models

Watson *et al.* (1981; hereafter model W) consider mass loss from a planet's hydrogen exosphere at 1 AU from a solar-type star (specifically, the Earth). Model W introduces the quantity S (erg cm⁻² s⁻¹), the sphere-averaged, efficiency-corrected areal heating rate in the planetary atmosphere due to XUV solar irradiation, such that

$$S = \int dh Q_0(h). \quad (6)$$

Here the integral is carried out over the height range h in the planetary thermosphere where $Q_0(h)$ is appreciable. Watson *et al.* find $S \sim 1$ erg cm⁻² s⁻¹, to be compared with the solar constant at Earth, 1.4×10^6 erg cm⁻² s⁻¹. Thus, the efficiency of XUV heating having already been incorporated in the definition of S , model W predicts $\varepsilon \sim 10^{-6}$, for a planet at 1 AU from the Sun, where tidal effects are negligible. We will employ this result, valid for a hydrogen exosphere at 1 AU from a 1-M_⊕ dwarf at an age of 4.5 Ga, to scale the results of model W to highly-irradiated EGPs.

Baraffe *et al.* (2004; hereafter model B) calculate a quantity (which they call F^*) equivalent to model W's S and obtain essentially the same value for Earth-like parameters: $S \sim 2 \text{ erg cm}^{-2} \text{ s}^{-1}$. However, their calculated loss rate Φ_B is $\sim 10^2 \Phi_W$, where Φ_W is the model W loss rate for the same irradiation parameters. We scale model B to model W by setting the efficiency factor for model B: $\varepsilon_B \sim 10^2 \varepsilon_W \sim 10^{-4}$.

The third model, Yelle's (2004; hereafter model Y), which does not incorporate tidal effects, gives the lowest efficiency factor: $\varepsilon_Y \sim 10^{-2} \varepsilon_W \sim 10^{-8}$. This result can be readily deduced from Yelle's Fig. 7, which plots $\Phi(a)$. Yelle notes that Φ is almost precisely proportional to a^{-2} , as would be expected for energy-limited escape.

Thus, the oldest mass-loss model, model W, is logarithmically almost exactly midway between models B and Y. In the following discussion, we calculate mass-loss histories for the three models, B, W, and Y, writing

$$\Phi_i = \tau \frac{\Phi_Y}{a^2} \frac{S(t)}{S(4.5 \text{ Ga})} \frac{\varepsilon_i}{\varepsilon_Y}. \quad (7)$$

In Eq. (7), a is in AU, and $S(t)$ is scaled to the value for the present Sun at age $t = 4.5$ Ga. Although the masses of the host stars of known highly-irradiated EGPs differ by modest factors from $1 M_\odot$, for the purposes of this paper we approximate all of these stars by the Sun. Particularly for the B model, the early history of $S(t)$ is important, and we approximate it by

$$\frac{S(t)}{S(4.5 \text{ Ga})} = \left(\frac{4.5 \text{ Ga}}{t} \right)^{0.85} \quad (8)$$

(Ribas *et al.*, 2005). This expression has a singularity at $t = 0$, meaning that there is a spike in mass loss at early epochs. However, the time integral of the mass loss rate is integrable, and we find that the EGP mass range where significant mass loss occurs is not strongly affected by the model for the early history of $S(t)$, for the Y and W models. In contrast, for a broad range of masses in the B model, a large fraction of the cumulative mass loss occurs when $t < 1$ Ga.

3. Coupling of mass loss models to interior evolution

We have prepared a grid of surface conditions for EGP evolution at four distances from the primary star, namely, 0.023 AU (OGLE-TR-56b), 0.034 AU, 0.046 AU (HD209458b; Brown *et al.* 2001, Schneider 2005), and 0.057 AU. The orbital radius $a = 0.034$ AU was chosen to correspond to a value midway between the orbits of OGLE-TR-56b and HD209458b. The orbital radius $a = 0.057$ AU was chosen to be spaced at the same interval as the previous three. It does not coincide with any particular EGP.

The method for computation of these grids is described in Burrows *et al.* (2004). In all cases the primary star is assumed to be the present-day Sun, a G2V dwarf at an age of 4.5 Ga. We recognize that this assumption introduces an inconsistency with Eq. (7), which means that the limits for stability of highly-irradiated EGPs derived below will be affected to the extent that the early mass loss is important. In most cases where this is true, other uncertainties, to be described below, are dominant. At a fixed distance to the star, the surface-condition grid is a table giving the asymptotic (deep interior) specific entropy, S/Nk as a function of the surface gravity g and the effective temperature T_{eff} . The EGP's "surface" is defined as the 1-bar level, and T_{eff} characterizes the *deep*

(intrinsic) heat flux, such that the latter is given by T_{eff}^4 multiplied by the Stefan-Boltzmann constant, σ . Here S/Nk is the entropy per baryon per Boltzmann's constant, computed using a solar-composition mixture of hydrogen and helium with the Saumon *et al.* equation of state (1995). When referring to the specific entropy, we always use the quantity S/Nk , which should not be confused with the areal heating rates S or S_* .

Moreover, the deposition of XUV energy, characterized by S , occurs high in the EGP atmosphere, affecting only the mass-loss rate. The bulk of the irradiation energy (which scales with S_* , $\gg S$) is deposited much deeper in the atmosphere and is incorporated, via the surface-condition grid, in $S/Nk(g, T_{\text{eff}})$.

One of the main objectives of this paper is to define the lower limit for stability to mass loss as a function of a . For the W and (in particular) the Y model, this limit is primarily determined by the tidal stripping criterion, i.e., the planetary radius r as compared with r_H . In the low mass range, close to the stability limit, one has $r \sim r_H$, but r is an increasing function of S/Nk . As the planet radiates deep-interior heat to space, S/Nk decreases. Thus the stability limit, basically determined by $\tau \rightarrow \infty$, is a function of the planet's initial S/Nk . It therefore turns out that the stability limit (for Y and W models) depends on the initial formation history of the EGP. To address this problem in a very approximate way, we assume that the EGP is initially formed during the first 10^6 years of the system's existence, at an initial orbital radius $> 1-10$ AU, where irradiation and tidal effects are negligible. We then assume that such an EGP subsequently migrates inward under the influence of torques from the protostellar nebula (Lin *et al.* 2000) and reaches its final orbital radius a by a system age $t \sim 1$ to 5 Ma, at which point the nebula and resulting torques have vanished. The initial S/Nk of the EGP is estimated by computing the approximate S/Nk of an isolated (non-irradiated) EGP of mass M at the specified age t . The implications of this calculation for the tidal mass limit are shown in Fig. 1, where the solid curve shows $\tau(M)$ for S/Nk corresponding to an age $t = 1$ Ma and the dotted curve corresponds to $t = 5$ Ma. This calculation is not intended to define the tidal stability limit with great exactitude, nor does it address the question of whether a solar-composition mass $< 0.2 M_J$ can be formed in the first place.

Obviously, the tidal enhancement factor becomes even less pronounced for the models at larger values of a . Figure 2 shows τ for $a = 0.034$ AU, and Fig. 3 shows τ at $a = 0.046$ AU (the orbital radius of HD 209458b, but for a $1 - M_\odot$ primary; the actual mass of HD 209458 is $1.05 M_\odot$).

4. Results

4.1. Boundary conditions

Figure 4 shows the surface-condition grids $S/Nk(g, T_{\text{eff}})$ for the four orbital radii, as calculated for a $1 - M_\odot$ primary at $t = 4.5$ Ga. Superimposed are evolutionary tracks for EGPs close to the stability limit. The model-atmosphere grids were constructed by using ~ 10 equally-spaced values of $\log g$ (cm s^{-2}) and T_{eff} (K) as independent variables and solving for the deep entropy. The resulting ~ 100 data points were then fitted with a smooth surface. As is evident from the evolutionary plots, some extrapolation was necessary for the extreme B models. In the case of low- g models ($\log g < 1.5$), the

assumption of a plane-parallel atmosphere becomes suspect; this problem primarily arises for low-mass models ($M \ll 1 M_J$) close to the stability limit. Since no calculations were performed for $T_{\text{eff}} < 50$ K, the S/Nk surface is truncated at very low values.

4.2. Stability limit

The term, “stability limit,” requires some discussion, since the physical mechanism for the non-persistence of EGPs due to mass loss varies with orbital radius a and efficiency factor ε . In general, our calculations do not exhibit a dynamical instability whereby a perturbation to the EGP, such as removal of an atmospheric mass layer, is self-accelerated, growing exponentially with time. A classical example of such behavior would be a gaseous sphere with a polytropic index greater than one, filling its Roche lobe in proximity to the primary star. For such an object, a decrease in mass M results in an increase of radius R and overflow of the Roche lobe at an accelerating rate. However, EGPs with $M \sim 1 M_J$ have effective polytropic indices close to unity, and so this instability only appears for $M \ll 1 M_J$. For the W models, the tidal limit is the operative one, and we do observe an abrupt instability, usually within mass and time ranges too fine to resolve, for masses where $\tau \rightarrow \infty$, as discussed in Section 2.1. For the B models, ε is so large that masses $M \sim 1 M_J$ suffer continual mass loss without exhibiting a dynamical instability. For the latter models, there is, strictly speaking, no mass limit defined by stability considerations. Our compromise definition of “stability limit,” which can be applied to all three mass-loss models, is that the limiting mass at orbital radius a is the initial mass which will decrease by a factor two over a time period of 5 Ga. In the case of the Y models, the fractional mass loss near the stability limit is almost a step function in M because of the influence of the τ factor.

In Fig. 4, evolution begins at the upper end of the curve, where the EGP of mass M is deposited at an age of 5 Ma. The model initially deflects to lower surface gravity, caused by the high initial XUV flux from the young host star and corresponding high mass loss, as given by Eq. (8). The EGP evolves downward to the final evolution point, which corresponds to $t = 5$ Ga, $M = 0$, or evolution to the surface’s truncation, whichever occurs first. In the case of Fig. 4 (a), for $a = 0.023$ AU, the initial masses that marginally disappear before 5 Ga are $2.8 M_J$ (model B), $0.47 M_J$ (model W), and $0.195 M_J$ (model Y). The result for the B model is generally consistent with the results presented by Baraffe *et al.* (2004). However, as is evident in Fig. 4 (a), the critical mass range for model B is so large that we must modestly extrapolate our $S/Nk(g, T_{\text{eff}})$ surface to larger values of g . The Y model’s critical mass is entirely determined by Roche-lobe overflow, which occurs at a mass between 0.195 and $0.200 M_J$. As would be expected, model W gives intermediate results.

Note in Fig. 4 that for the Y model, mass loss is so slow that all of the models show increasing surface gravity as a result of contraction, despite mass loss. This is also true for the two most massive W models (0.35 and $0.40 M_J$), while the $0.30 M_J$ W model sheds mass at a sufficiently rapid rate to disappear within 5 Ga. Thus, in the case of the W model at this orbital distance, one Saturn mass is at the stability limit. The B models all show decreasing surface gravity with time as mass loss is substantial throughout their evolution.

4.3. Mass loss and radius variations

In Fig. 5, we plot the $M(t)$ trajectories for the B models plotted in Fig. 4. The cusp in $M(t)$ as $t \rightarrow 0$ is a consequence of Eq. (8). Figure 6 shows the evolution of radius with time, for the same models plotted in Fig. 5 (mass-loss model B).

Note that one of the $M(t)$ and $R(t)$ trajectories plotted in Figs. 5 and 6 terminates at $t = 3.9$ Ga. Fortunately, the parameters for this model, $a = 0.046$ AU and initial mass $M = 1.1 M_J$, allow us to resolve a tidal instability. Just as the EGP decreases to a mass of $0.15 M_J$, its effective polytropic index increases to a sufficiently large value for the radius to expand with further mass loss, leading to rapid Roche-lobe overflow.

Figure 7 shows $M(t)$ trajectories for the W models plotted in Fig. 4. Curves which terminate before $t = 5$ Ga reach the tidal instability limit. Note that the ordinate range is much smaller than in Fig. 5. As in the case of the B model, there is a cusp in the early $M(t)$ curves due to high initial XUV irradiation, but its net effect is merely to shift the critical initial mass upward by perhaps ten percent.

Figure 8 shows the evolution of radius with time, for the same models plotted in Fig. 7 (mass-loss model W). Figure 9 shows $M(t)$ trajectories for the Y models plotted in Fig. 4. The plots terminate at $t = 1$ Ga because little change is seen except for models which reach the tidal instability limit at earlier times. All masses are below the mass of Saturn. Thus, in the Y model, significant mass loss due to irradiation could only occur in very low-mass hydrogen-rich giant planets. Figure 10 shows the evolution of radius with time, for the same models plotted in Fig. 9 (mass-loss model Y).

As has already been emphasized by Baraffe *et al.* (2004), if mass-loss model B is correct, HD 209458b would have to be a remnant of a substantially more massive object. For the W model at the distance of HD 209458b, rapid cooling causes a rapid increase of surface gravity despite mass loss, and the marginal model is only $\sim 50\%$ more massive than Neptune (Neptune's mass $M = 0.05 M_J$). Determination of the radius of a Neptune-mass EGP might help to resolve whether predominantly-hydrogen objects of such low mass exist. However, the absence of an example of a Neptune-mass hydrogen planet might not be so much a test of mass-loss theories as a constraint on formation mechanisms for small hydrogen objects.

As we see, the B model implies that one Jupiter mass can persist for 5 Ga as an EGP at $a = 0.057$ AU, but only marginally, and with substantially-reduced mass at 5 Ga. For the W model, the stability limit is at ~ 3 Neptune masses. For the Y model, the limit is at about a Neptune mass.

5. Discussion

Figures 11 and 12 summarize the principal results of our calculations. In Fig. 11, the ordinate represents the initial mass of an EGP whose mass will be reduced by a factor of ~ 2 after 5 Ga. For the B models, the limit is primarily established by the very large value $\varepsilon_B \sim 10^{-4}$. For the Y models, tidal truncation is the most important factor, especially for the smallest values of a , and models close to the stability limit disappear within $t \ll 5$ Ga. The W models are intermediate. Also shown in Fig. 11 are data points for transiting EGPs, as well as lower mass limits for highly-irradiated EGPs of unknown orbital inclination. The data points (see also Schneider 2005) are (in order of increasing a)

Gliese 876d (green square and arrow; Rivera *et al.* 2005), OGLE-TR-56b (Bouchy *et al.* 2005), OGLE-TR-113b (arrow; Bouchy *et al.* 2004), GJ 436b (green square and arrow; Butler *et al.* 2004), OGLE-TR-132b (Bouchy *et al.* 2004), HD 63454b (arrow; Moutou *et al.* 2005), HD 73256b (arrow; Udry *et al.* 2003), 55 Cnc e (black square and arrow; McArthur *et al.* 2004), TrES-1 (Alonso *et al.* 2004), OGLE-TR-10b (Bouchy *et al.* 2005), HD 46375b (arrow; Marcy *et al.* 2000), HD 149026b (Sato *et al.* 2005), HD 209458b (Brown *et al.* 2001), OGLE-TR-111b (Pont *et al.* 2005), and HD 49674b (black square and arrow; Butler *et al.* 2003).

Comparison of these data points with our results from applying the three theories indicates that if the extreme B model were correct, virtually all observed hot EGPs must be remnants of much more massive bodies, originally several times Jupiter and still losing substantial mass fractions at present. Because the mass-loss rate in the B theory is so extreme, a large fraction of the cumulative mass loss occurs for $t \ll 1$ Ga, when the young primary star has a large XUV flux.

Implications of the W and Y theories are very different (see Fig. 12): observed hot EGPs retain practically all of the nebular-gas mass fraction with which they were formed. There is an interesting difference between the W and Y theories that is potentially testable from observations: the W theory predicts that no Saturn-mass, hydrogen-dominated EGPs should be observed with orbital radii less than about 0.05 AU (for solar-type primaries), while such objects could exist if the Y theory is correct. If the B theory is correct, Saturn-mass EGPs within ~ 0.1 AU of their primaries could exist only for a brief interval on their way to complete evaporation.

The observations by Vidal-Madjar (2003) of an extended hydrogen atmosphere around HD209458b provide an observational constraint on Φ for this object, but not a direct determination. Yelle (2004) estimates $\Phi_Y \sim 5 \times 10^{10}$ molecules $\text{cm}^{-2} \text{ s}^{-1}$ for his reference model, intended to correspond to HD209458b. As discussed by Yelle, Vidal-Madjar *et al.* claim that $\Phi \sim 5 \times 10^{12}$ molecules $\text{cm}^{-2} \text{ s}^{-1}$ (~ 100 times larger than Φ_Y) is required to explain HD209458b's extended atmosphere. Thus, Vidal-Madjar's interpretations of their observations imply a mass-loss flux in the same range as model W, while Yelle's detailed model (Y) of the same object predicts a flux two orders of magnitude lower.

For even the most conservative mass loss theory (Y), the \sim Neptune-mass planets Gliese 876d, GJ 436b, and 55 Cnc e are unlikely to be composed primarily of hydrogen. This conclusion must be confirmed by further calculations, however, because Gliese 876 and GJ 436 are M dwarfs rather than G dwarfs, so their EGP mass flux due to irradiation must be scaled accordingly.

Acknowledgments

This research was supported by NASA Grant NAG5-13775 (PGG) and NASA Grants NNG04GL22G and NNG05GG05G (ATP).

References

Alonso , R., Brown, T.M., Torres, G., Latham, D.W., Sozzetti, A., Mandushev, G., Belmonte, J.A., Charbonneau, D., Deeg, H.J., Dunham, E.W., O'Donovan, F.T., Stefanik, R.P. 2004. TrES-1: The transiting planet of a bright K0 V star. *Astrophys. J.* 613, L153-L156.

Baraffe, I., Selsis, F., Chabrier, G., Barman, T.S., Allard, F., Hauschildt, P.H., Lammer, H., 2004. The effect of evaporation on the evolution of close-in giant planets. *A&A* 419, L13-L16.

Bouchy, F., Pont, F., Santos, N.C., Melo, C., Mayor, M., Queloz, D., Udry, S., 2004. Two new "very hot Jupiters" among the OGLE-TRansiting candidates. *A&A* 421, L13-L16.

Bouchy, F., Pont, F., Melo, C., Santos, N.C., Mayor, M., Queloz, D., Udry, S., 2005. Doppler follow-up of OGLE-TRansiting companions in the Galactic bulge. *A&A* 431, 1105-1121.

Brown, T.M., Charbonneau, D., Gilliland, R.L., Noyes, R.W., Burrows, A., 2001. Hubble Space Telescope Time-Series Photometry of the Transiting Planet of HD 209458. *Astrophys. J.* 552, 699-709.

Burrows, A., Hubeny, I., Hubbard, W.B., Sudarsky, D., Fortney, J.J., 2004. Theoretical radii of transiting giant planets: the case of OGLE-TR-56b. *Astrophys. J.* 610, L53-L56.

Butler, R.P., Vogt, S.S., Marcy, G.W., Fischer, D.A., Wright, J.T., Henry, G.W., Laughlin, G., Lissauer, J.J., 2004. A Neptune-mass planet orbiting the nearby M Dwarf GJ 436. *Astrophys. J.* 617, 580-588.

Butler, R.P., Marcy, G.W., Vogt, S.S., Fischer, D.A., Henry, G.W., Laughlin, G., Wright, J.T., 2003. Seven New Keck Planets orbiting G and K Dwarfs. *Astrophys. J.* 582, 455-466.

Jaritz, G. F., Endler, S., Langmayr, D., Lammer, H., Grießmeier, J.-M., Erkaev, N. V., Biernat, H. K., 2005. Roche lobe effects on expanded upper atmospheres of short-periodic giant exoplanets. *A&A* 439, 771-775.

Lammer, H., Selsis, F., Ribas, I., Guinan, E.F., Bauer, S.J., Weiss, W.W., 2003. Atmospheric loss of exoplanets resulting from stellar X-ray and extreme-ultraviolet heating. *Astrophys. J.* 598, L121-L124.

Lin, D.N.C., Papaloizou, J.C.B., Terquem, C., Bryden, G., Ida, S. 2000. Orbital evolution and planet-star tidal interaction. In: Mannings, V., Boss, A.P., Russell, S.S. (Eds.), *Protostars and Planets IV*. University of Arizona Press, Tucson, pp. 1111-1134.

Marcy, G.W., Butler, R.P., Vogt, S.S., 2000. Sub-Saturn planetary candidates of HD 16141 and HD 46375. *Astrophys. J.* 536, L43-L46.

McArthur, B.E., Endl, M., Cochran, W.D., Benedict, G.F., Fischer, D.A., Marcy, G.W., Butler, R.P., Naef, D., Mayor, M., Queloz, D., Udry, S., Harrison, T.E., 2004. Detection of a Neptune-Mass planet in the ρ^1 Cancri system using the Hobby-Eberly telescope. *Astrophys. J.* 614, L81-L84.

Moutou, C., Mayor, M., Bouchy, F., Lovis, C., Pepe, F., Queloz, D., Santos, N., Sosnowska, D., Udry, S., Benz, W., Naef, D., Segresan, D., Sivan, J.-P., 2005. The HARPS search for southern extra-solar planets. IV. Three close-in planets around HD 2638, HD 27894 and HD 63454. *A&A*, submitted.

Pont, F., Bouchy, F., Melo, C., Santos, N.C., Mayor, M., Queloz, D., Udry, S., 2005. Doppler follow-up of OGLE planetary transit candidates in Carina. *A&A* 438, 1123-1140.

Ribas, I., Guinan, E. F., Güdel, M., Audard, M., 2005. Evolution of the Solar Activity over Time and Effects on Planetary Atmospheres. I. High-Energy Irradiances (1-1700 Å). *Astrophys. J.* 622, 680-694.

Rivera, E., Lissauer, J., Butler, P., Marcy, G., Vogt, S., Fischer, D., Brown, T., Laughlin, G., 2005. A ~ 7.5 Earth-mass planet orbiting the nearby star, GJ 876. *Astrophys. J. Lett.*, submitted.

Sato, B., Fischer, D., Henry, G., Laughlin, G., Butler, P., Marcy, G., Vogt, S., Bodenheimer, P., Ida, S., Toyaota, E., Wolf, A., Valenti, J., Boyd, L., Johnson, J., Wright, J., Ammons, M., Robinson, S., Strader, J., McCarthy, Ch., Tah, K., Minniti, D., 2005. The N2K Consortium. II. A Transiting Hot Saturn Around HD 149026 With a Large Dense Core. *Astrophys. J.*, accepted.

Saumon, D., Chabrier, G., Van Horn, H., 1995. An equation of state for low-mass stars and giant planets. *Astrophys. J. Suppl.* 99, 713-741.

Schneider, J. 2005. The Extrasolar Planets Encyclopaedia. <http://www.obspm.fr/planets>

Udry, S., Mayor, M., Clausen, J.V., Freyhammer, L.M., Helt, B.E., Lovis, C., Naef, D., Olsen, E.H., Pepe, F., Queloz, D., Santos, N.C., 2003. The CORALIE survey for southern extra-solar planetsX. A hot Jupiter orbiting HD73256. *A&A* 407, 679-684.

Vidal-Madjar, A., Lecavelier des Etangs, A., Desert, J.-M., Ballester, G.E., Ferlet, R., Hébrard, G.H., Mayor, M., 2003. An extended upper atmosphere around planet HD209458b. *Nature* 422, 143-146.

Watson, A.J., Donahue, T.M., Walker, J.C.G., 1981. The dynamics of a rapidly escaping atmosphere: application to the evolution of Earth and Venus. *Icarus* 48, 150–166.

Yelle, R.V., 2004. Aeronomy of extra-solar giant planets at small orbital distances. *Icarus* 170, 167–179.

Figures and Captions

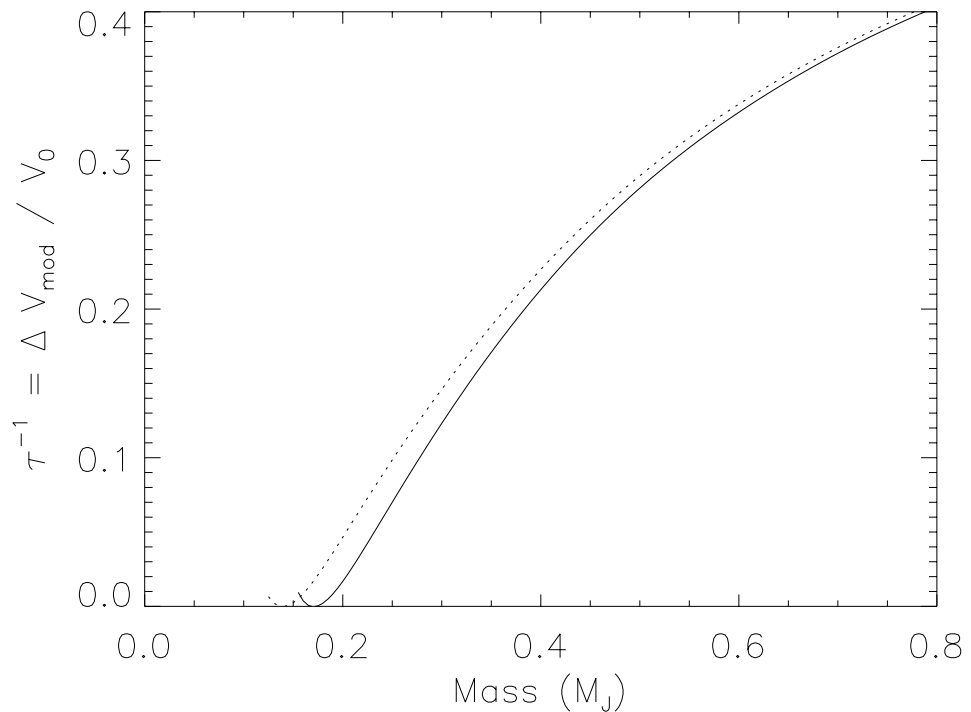


Fig. 1 – Reciprocal of the tidal enhancement factor for masses close to the tidal limiting mass (the mass for which the ordinate goes to zero), for a $1-M_\odot$ star and $a = 0.023$ AU. See text for further explanation.

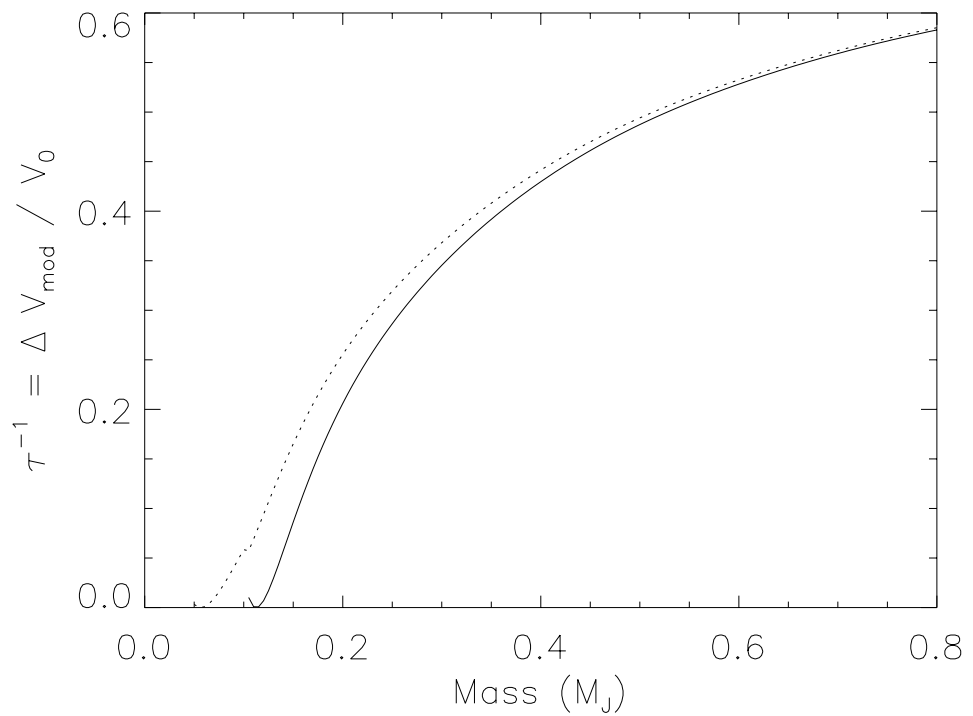


Fig. 2 – Reciprocal of the tidal enhancement factor for masses close to the tidal limiting mass (the mass for which the ordinate goes to zero), for a $1 - M_{\odot}$ star and $a = 0.034$ AU.

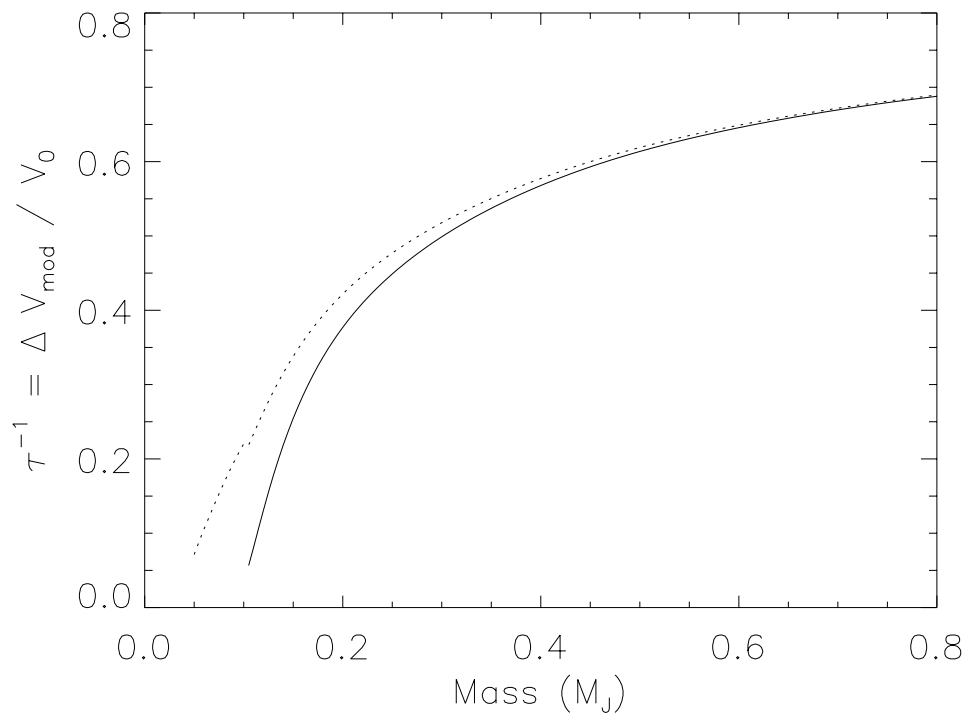


Fig. 3 – Reciprocal of the tidal enhancement factor for masses close to the tidal limiting mass (the mass for which the ordinate goes to zero), for a $1 - M_{\odot}$ star and $a = 0.046$ AU.

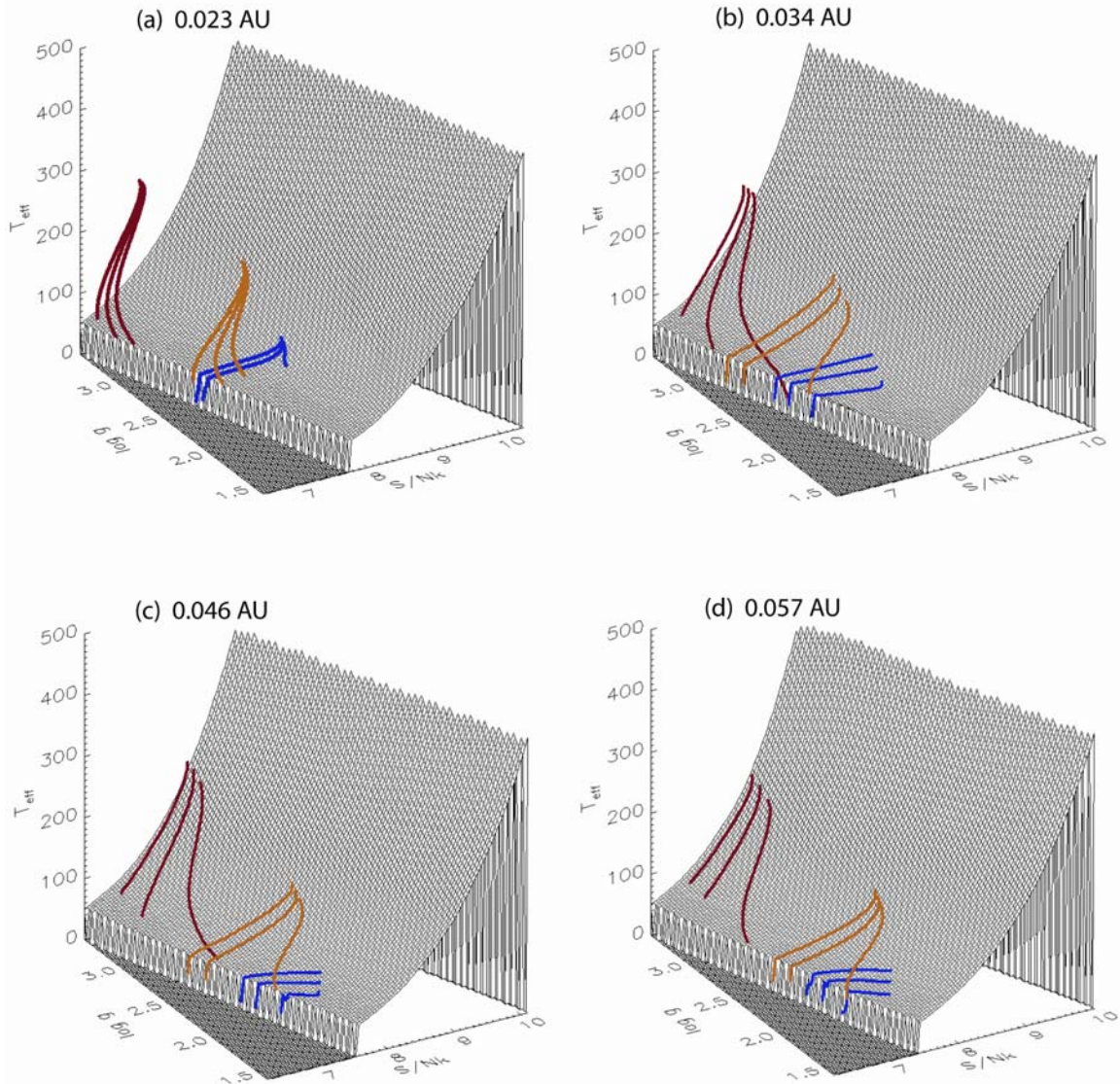


Fig. 4 – Evolution of EGPs on the $S/Nk(g, T_{\text{eff}})$ surface, for mass-loss models B (red), W (gold), and Y (blue), for the four semimajor axes studied in this paper. The masses plotted approximately straddle the mass limit. See text for details.

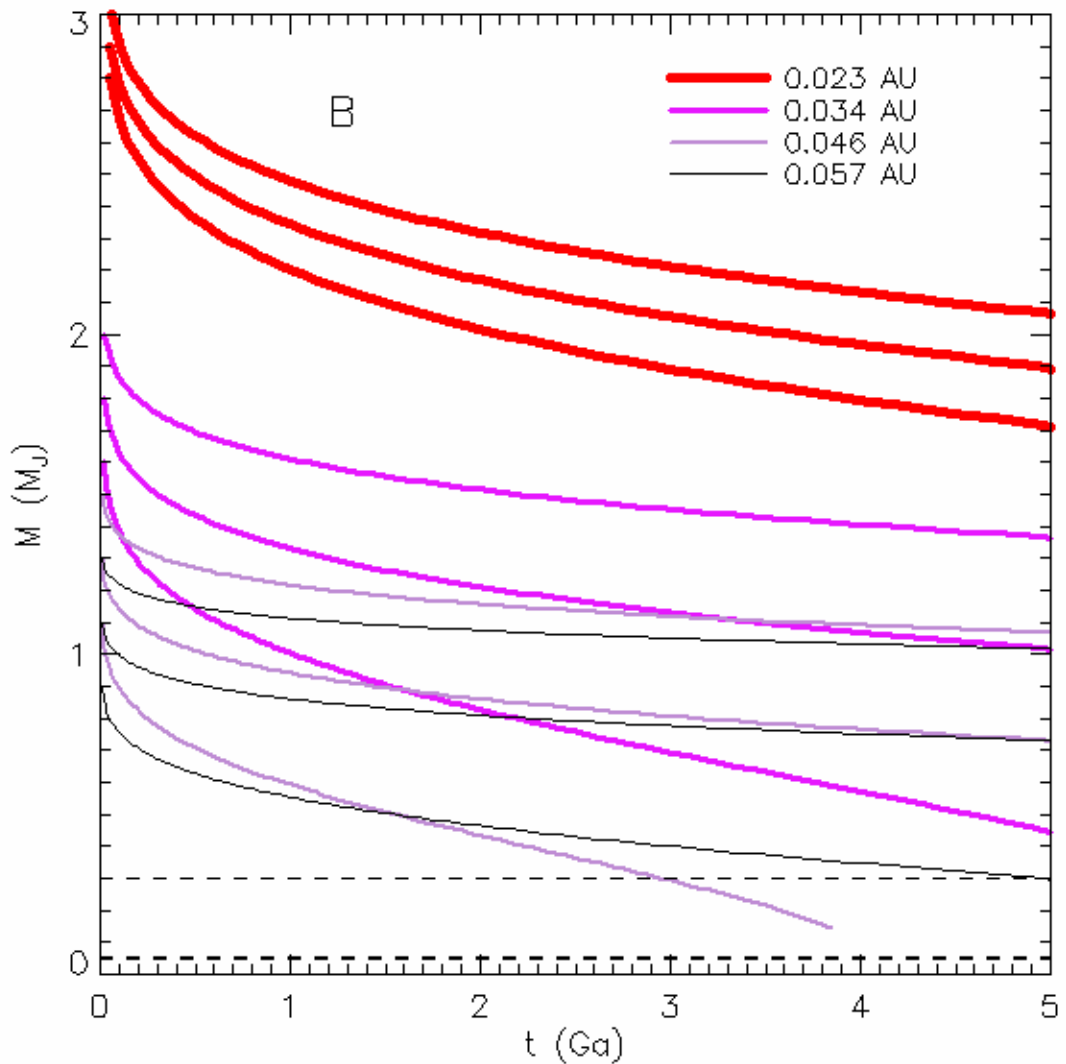


Fig. 5 – Model B predictions of mass with time for EGPs straddling the limiting mass, for the four values of a . The thickest lines correspond to the hottest EGPs at $a = 0.023$ AU, while the thinnest lines correspond to $a = 0.057$ AU. Horizontal dashed lines are at the masses of Saturn and of Neptune and Uranus.

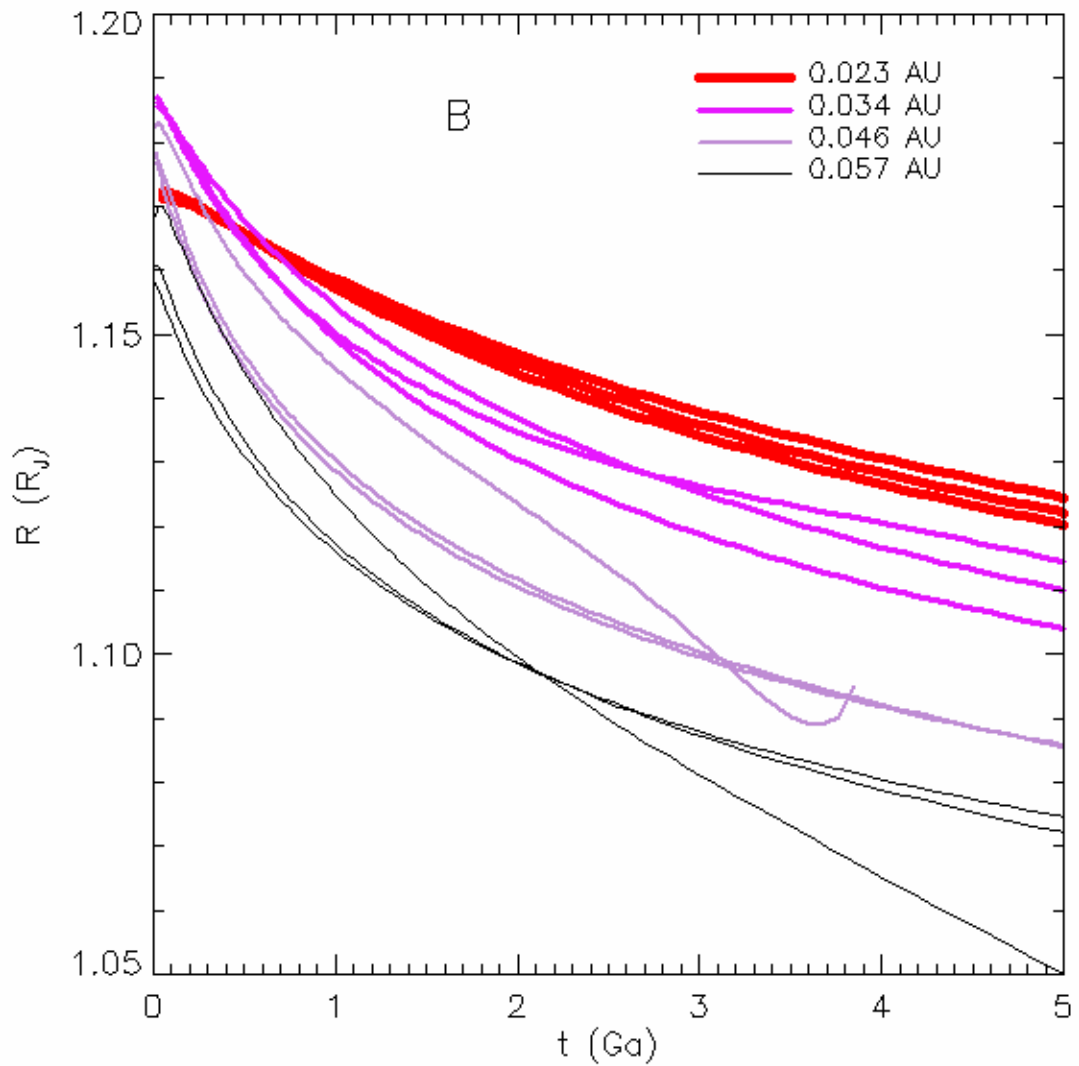


Fig. 6 – Model B predictions of radius with time for EGPs straddling the limiting mass, for the four values of a . One of the models (discussed in text) exhibits a tidal instability.

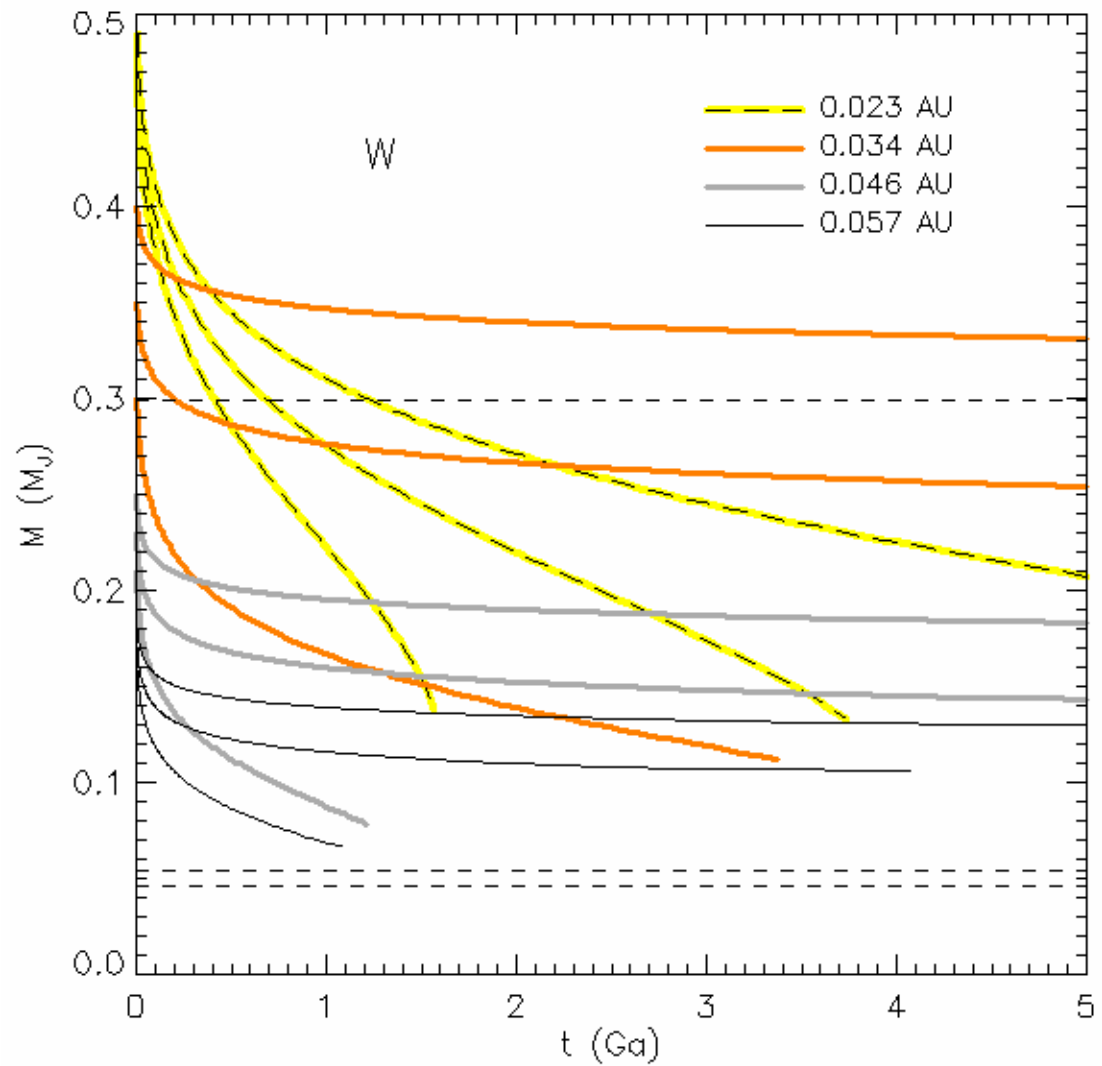


Fig. 7 – Model W predictions of mass with time for EGPs straddling the limiting mass, for the four values of a . The thick yellow lines correspond to the hottest EGPs at $a = 0.023$ AU, while the thinnest lines correspond to $a = 0.057$ AU. Horizontal dashed lines are at the masses of Saturn and of Neptune and Uranus.

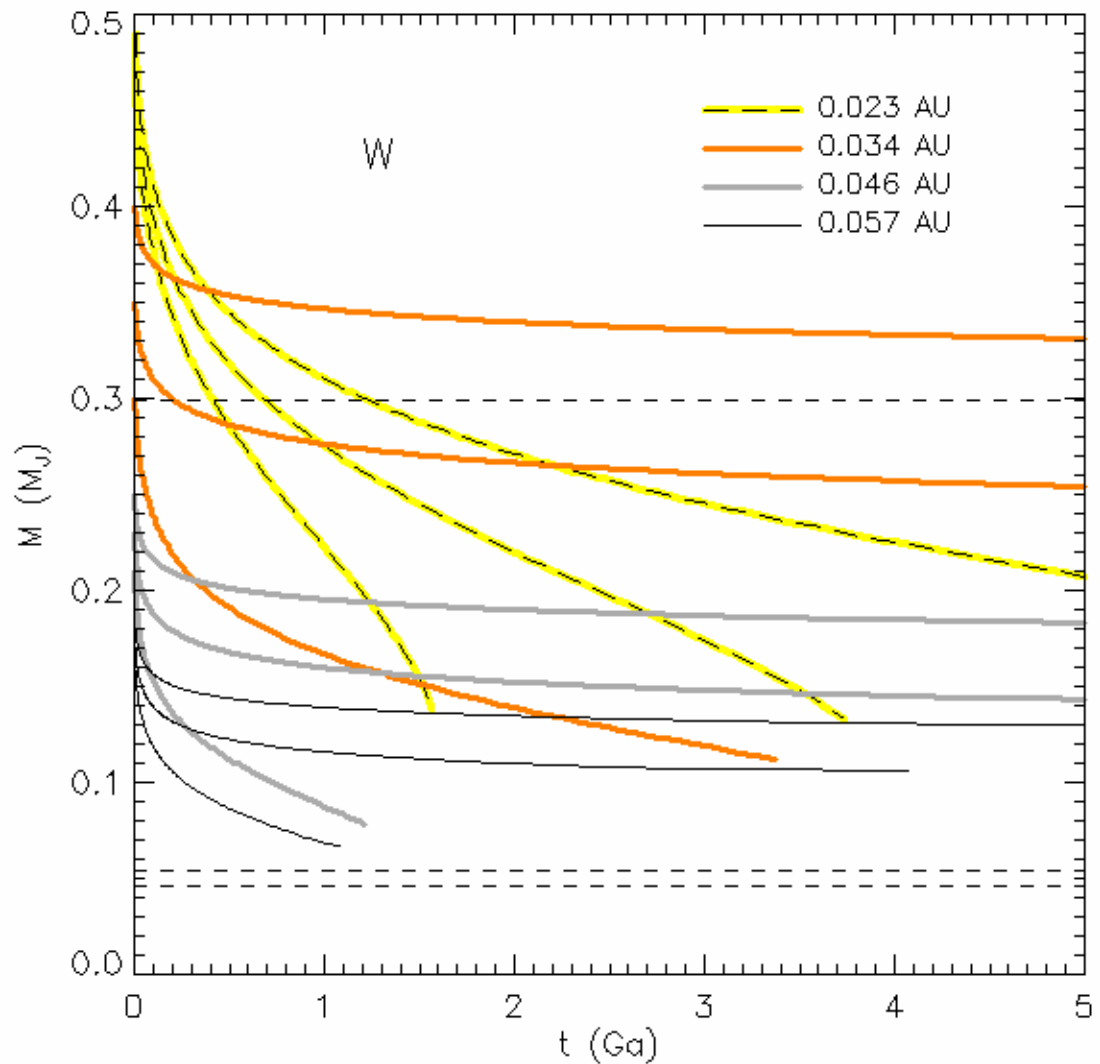


Fig. 8 – Model W predictions of radius with time for EGPs straddling the limiting mass, for the four values of α . The curves show the complex effects of initial high mass loss, Eq. (8), changing polytropic index, and tidal instability in several cases.

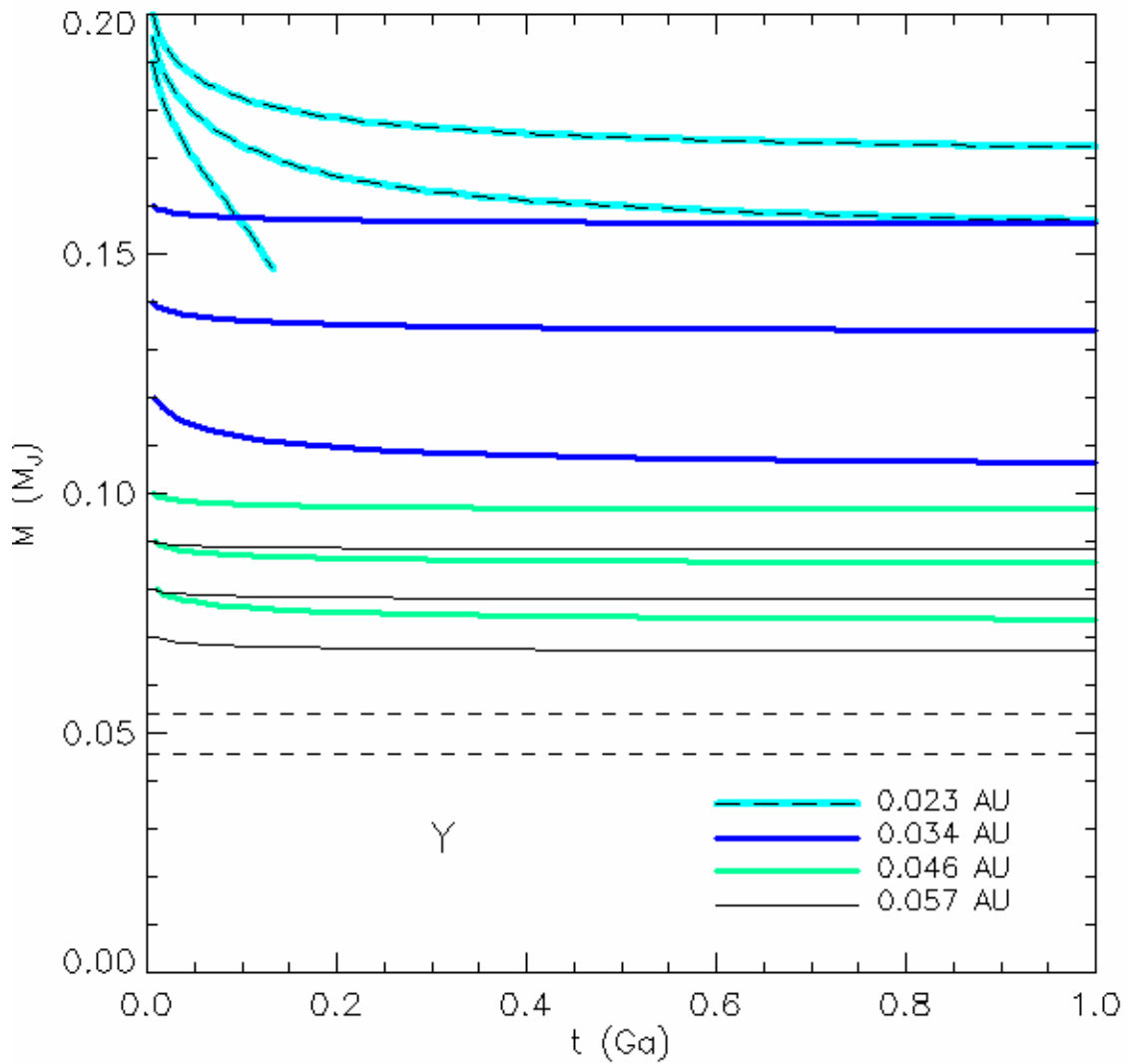


Fig. 9 – Model Y predictions of mass with time for EGPs straddling the limiting mass, for the four values of a . The thick aqua lines correspond to the hottest EGPs at $a = 0.023$ AU, while the thinnest lines correspond to $a = 0.057$ AU. Horizontal dashed lines are at the masses of Neptune and Uranus.

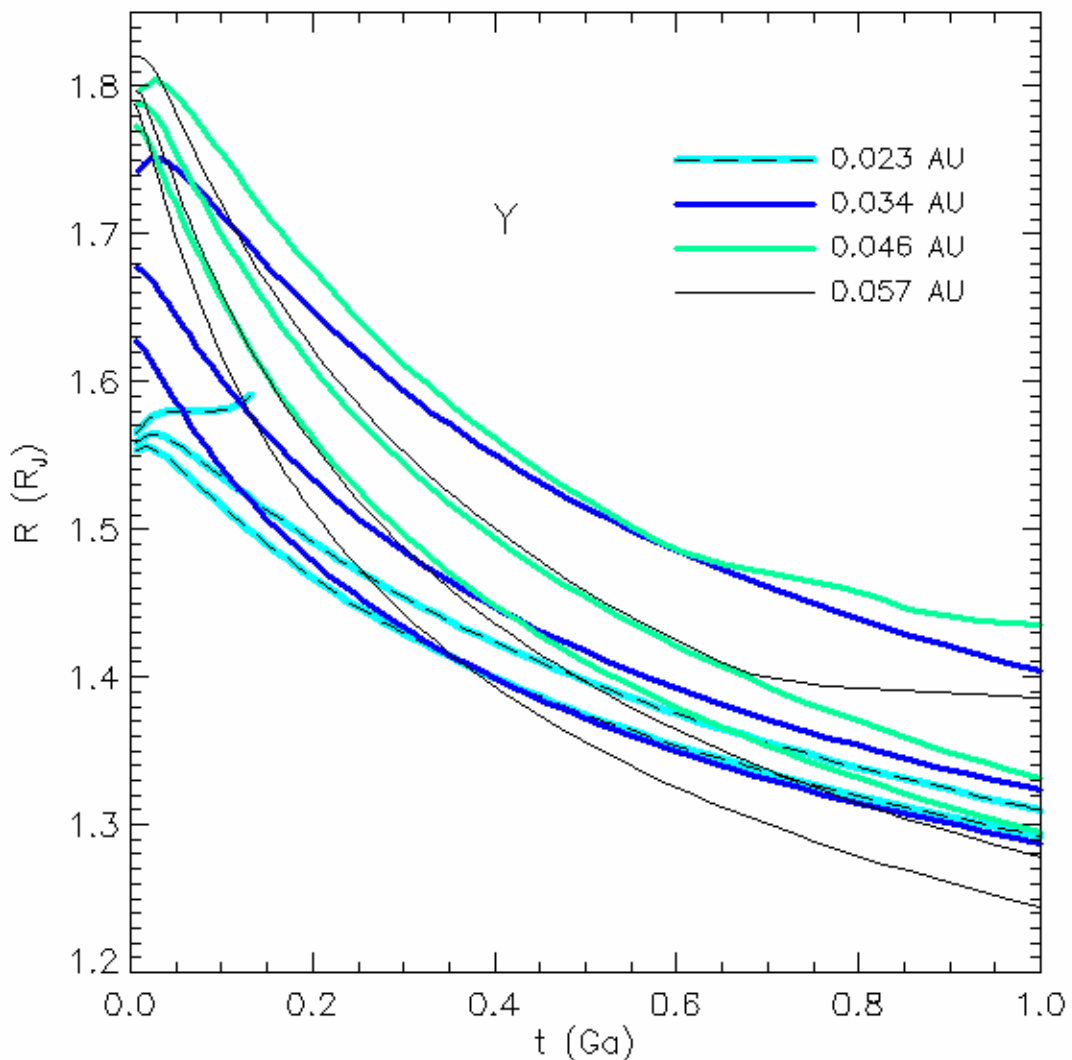


Fig. 10 – Model Y predictions of radius with time for EGPs straddling the limiting mass, for the four values of α . The curves show the complex effects of initial high mass loss, Eq. (8), changing polytropic index, and tidal instability.

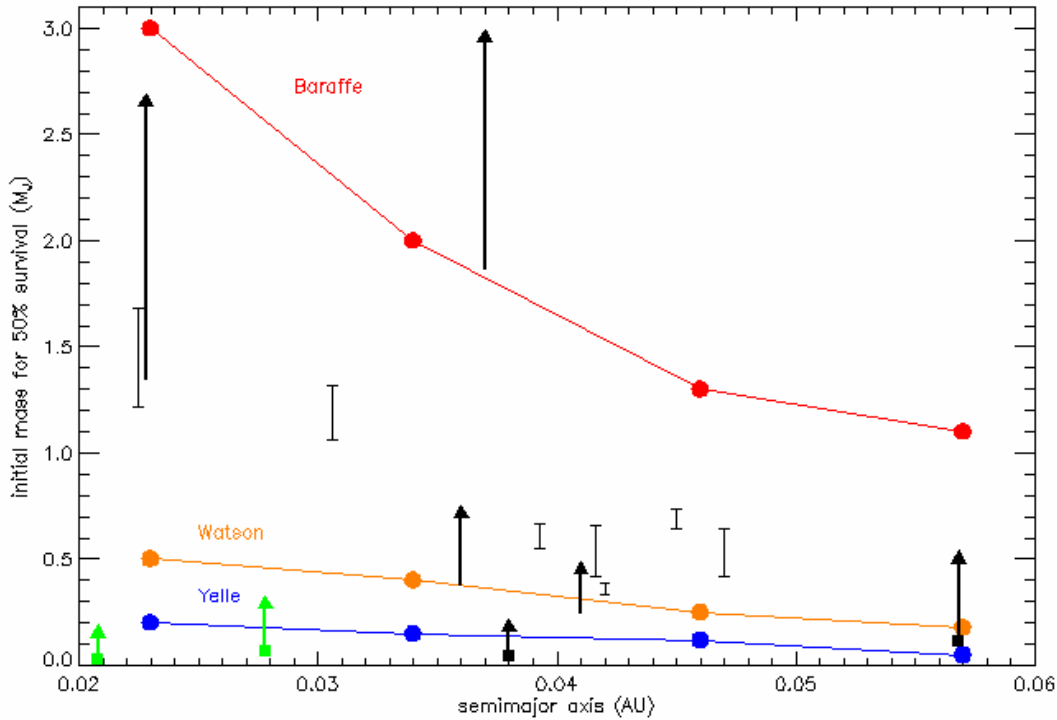


Fig. 11 – Limiting mass for stability of EGPs orbiting a solar-type star at various orbital distances, for the three mass-loss models. Observed EGPs are plotted for comparison, as black error bars (showing mass limits), black arrows (showing lower limit on mass; upper end of arrow has no significance), or as squares with arrows in the case of objects with probable masses in the range $\sim 0.05 M_J$ (Neptune or Uranus mass). In the case of the two data points shown as green squares with arrows, the primary has a mass ~ 0.3 – $0.4 M_\odot$, and the stellar XUV flux will be much lower than assumed by the scaling relations used in this paper.

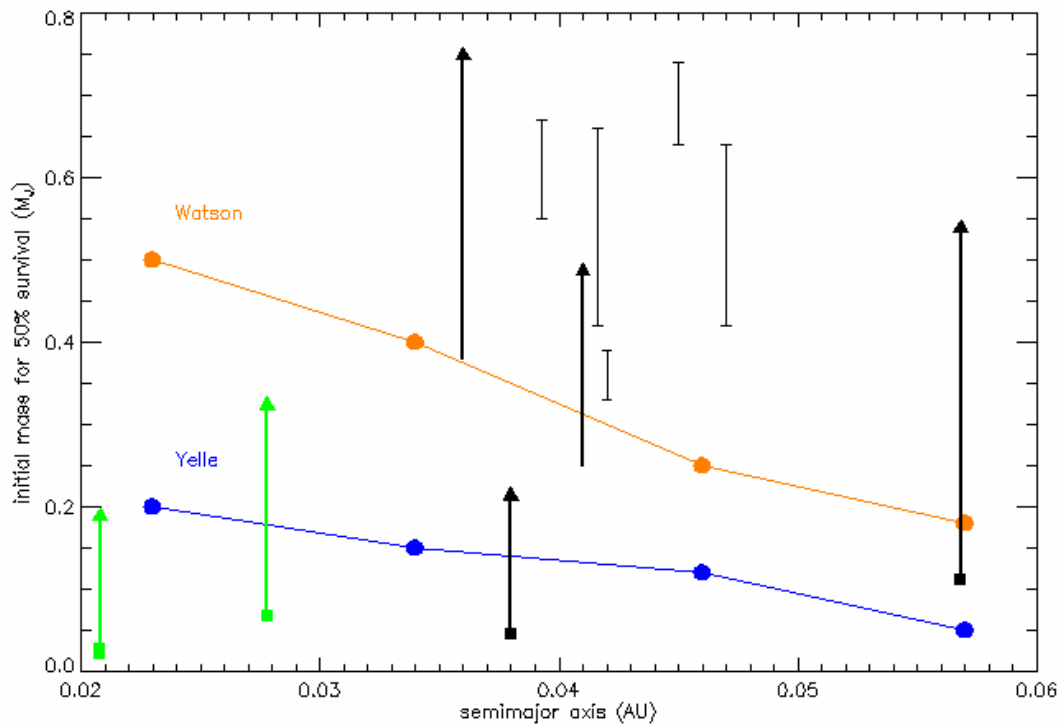


Fig. 12 – Enlarged view of the lower portion of Fig. 11.